

Quasi-phase-matched up- and down-conversion in periodically poled layered semiconductors

Chiara Trovatello^{1,2,*}, Carino Ferrante³, Birui Yang⁴, Josip Bajo⁵, Benjamin Braun⁵, Xinyi Xu¹, Zhi Hao Peng¹, Philipp K. Jenke⁵, Andrew Ye⁶, Milan Delor⁷, D. N. Basov⁴, Jiwoong Park^{6,8,9}, Philip Walther^{5,10}, Lee A. Rozema⁵, Cory Dean⁴, Andrea Marini^{3,11}, Giulio Cerullo^{2,*} and P. James Schuck^{1,*}

¹*Department of Mechanical Engineering, Columbia University, New York, NY 10027, USA*

²*Dipartimento di Fisica, Politecnico di Milano, Piazza L. da Vinci 32, I-20133 Milano, Italy*

³*CNR-SPIN, c/o Dip.to di Scienze Fisiche e Chimiche, Via Vetoio, Coppito (L'Aquila) 67100, Italy*

⁴*Department of Physics, Columbia University, New York, NY 10027, USA*

⁵*University of Vienna, Faculty of Physics, Vienna Center for Quantum Science and Technology (VCQ) & Research Network Quantum Aspects of Space Time (TURIS), 1090 Vienna, Austria*

⁶*Pritzker School of Molecular Engineering, University of Chicago, Chicago, IL, USA*

⁷*Department of Chemistry, Columbia University, New York, NY 10027, USA*

⁸*James Franck Institute, University of Chicago, Chicago, IL, USA*

⁹*Department of Chemistry, University of Chicago, Chicago, IL, USA*

¹⁰*Christian Doppler Laboratory for Photonic Quantum Computer, Faculty of Physics, University of Vienna, 1090 Vienna, Austria*

¹¹*Department of Physical and Chemical Sciences, University of L'Aquila, Via Vetoio, 67100 L'Aquila, Italy*

**Corresponding authors. Email: ct2938@columbia.edu, giulio.cerullo@polimi.it, p.j.schuck@columbia.edu*

Nonlinear optics lies at the heart of classical and quantum light generation[1–3]. The invention of periodic poling revolutionized nonlinear optics and its commercial applications by enabling robust quasi-phase-matching in crystals such as lithium niobate[3, 4]. However, reaching useful frequency conversion efficiencies requires macroscopic dimensions, limiting further technology development and integration. Here we realize a periodically poled van der Waals semiconductor (3R-MoS₂)[5–7]. Due to its exceptional nonlinearity, we achieve macroscopic frequency conversion efficiency over a microscopic thickness of only 1.2 μm, 10 – 100× thinner than current systems with similar performances[3, 8, 9]. Due to unique intrinsic cavity effects, the thickness-dependent quasi-phase-matched second harmonic signal surpasses the usual

quadratic enhancement by 50%. Further, we report the broadband generation of photon pairs at telecom wavelengths via quasi-phase-matched spontaneous parametric down-conversion. This work opens the new and unexplored field of phase-matched nonlinear optics with microscopic van der Waals crystals, unlocking applications that require simple, ultra-compact technologies such as on-chip entangled photon-pair sources for integrated quantum circuitry and sensing [2, 3, 10].

The inherent nonlinear response of matter to external electromagnetic stimuli allows photons of different frequencies incident on a material to interact with each other, enabling a myriad of photonic applications such as frequency conversion and the generation of non-classical states of light. Particularly interesting are second-order nonlinear processes, which occur in non-centrosymmetric media with $\chi^{(2)} \neq 0$ and are used to produce new light frequencies *e.g.*, in second harmonic generation (SHG), sum and difference frequency generation, and entangled photon pairs in spontaneous parametric down-conversion (SPDC)[1, 11].

Efficient nonlinear frequency conversion is achieved by fulfilling the so-called phase matching (PM) condition, which implies a zero wave-vector mismatch - *i.e.*, momentum conservation - for the interacting waves ($\Delta k = 0$). For both SHG and SPDC, $\Delta k = k_{2\omega} - 2k_{\omega} = \frac{2\omega}{c}(n_{2\omega} - n_{\omega})$ and PM requires matching the refractive indexes of the fundamental wavelength (FW), n_{ω} , and of the second harmonic (SH), $n_{2\omega}$. In the absence of PM, the conversion efficiency reaches its maximum for a propagation distance corresponding to the coherence length $L_c = \pi/\Delta k$ and then oscillates with period $2L_c$ [1]. Birefringent phase-matching (BPM) exploits the optical anisotropy of non-centrosymmetric nonlinear crystals by adjusting the propagation direction inside the crystal so that the fields at ω and 2ω with different polarizations experience the same refractive index. For SHG with BPM, the SH intensity $I_{2\omega}$ grows quadratically with the thickness L of the nonlinear medium. While BPM is simple and effective, it can only be applied to a limited number of crystals, such as the prototypical β -barium borate (BBO), which display moderate $\chi^{(2)}$ values of a few pm/V[1].

There are many crystals with high nonlinearity but low anisotropy, *e.g.*, gallium arsenide (GaAs), for which BPM is not achievable. An alternative to BPM is quasi-phase-matching (QPM), which introduces periodic phase shifts of π between the fields at the FW and the SH at every coherence length L_c , restoring the proper phase relationship and the quadratic growth of the SH intensity with propagation length[4, 12].

Such a phase shift can be obtained by periodic inversion of the crystallographic orientation during material growth via molecular beam epitaxy[13–15], or by cleaving the nonlinear medium slabs along the different crystal planes and diffusion-bonding them into monolithic stacks[15–17]. In ferroelectric crystals

like lithium niobate (LN)[18, 19], lithium tantalate [20] or potassium titanyl phosphate [21], QPM can be achieved by periodic poling, *i.e.*, by periodically inverting the sign of the nonlinear coefficient $\chi^{(2)}$ upon high-voltage switching of ferroelectric domains following lithographic patterning of the electrodes[22]. The spatial modulation of $\chi^{(2)}$, which follows the electrode spacing, is the so-called poling period, and it determines the wavelengths for which a certain nonlinear process can be phase matched. For LN, the typical values of the poling periods are between 5 and 50 μm and the modulation can be extended over crystal thicknesses from millimeters to centimeters[22].

The invention of QPM was a breakthrough in nonlinear optics because it enabled the use of nonlinear crystals with large $\chi^{(2)}$ of the order of 10-20 pm/V, for which BPM cannot be achieved[3]. Periodically poled LN (PPLN) crystals provide the highest conversion efficiency for waveguided SHG ($I_{2\omega}/I_{\omega} \approx 70\%$)[8, 9], optical parametric amplifiers and oscillators[23–26] and entangled photon sources[27, 28]. Along with their high conversion efficiencies, standard nonlinear crystals like PPLN can be directly fabricated on silicon-based optical circuits, though their millimeter-to-centimeter thickness limits the number of devices that can be integrated on a single chip. This has spurred recent advances in the development of nonlinear metasurfaces[10, 29–32], thin films[33] and nanowaveguides[34], which are now leading a paradigm shift towards more miniaturized, and more tunable, nonlinear optical device platforms.

The rise of quantum and two-dimensional (2D) material science[35–40] has inspired research on less traditional classes of optical crystals including semiconducting transition metal dichalcogenides (TMDs), *e.g.*, MoS₂, MoSe₂, WS₂ and WSe₂. These are layered materials comprised of crystalline sheets with strong in-plane covalent bonds but weak out-of-plane van der Waals interactions. Starting from the first reports of SHG[41–43], their exceptional optical nonlinearities ($\chi^{(2)} = 100 - 1000$ pm/V), 100-1000x higher than standard bulk crystals due in part to favourable quantum geometries, have recently been exploited to demonstrate nonlinear effects at the ultimate thin-ness limit in single-layer TMDs[44–47]. However, in such cases, the overall conversion efficiency is still limited by the sub-nm propagation length[48]. In contrast to the most common 2H crystallographic phase, which is centrosymmetric in the bulk ($\chi^{(2)} = 0$), the 3R polytype is non-centrosymmetric ($\chi^{(2)} \neq 0$) and can be used to boost the conversion efficiency of second-order nonlinear optical processes by increasing the number of layers N in the TMD sample. Using thin 3R-MoS₂ flakes (1-6 layers), it has been shown that the SH intensity grows quadratically with the number of layers, *i.e.*, with the thickness of the nonlinear medium ($I_{\text{SHG}} \propto N^2$)[5].

However, when the number of layers is increased to $\sim 200 - 300$, the wave vector mismatch Δk results in an inevitable deviation from the N^2 enhancement[6, 7], and the SH oscillates with the sample thickness,

with a semi-period equal to the coherence length L_c [1]. Recently, the coherence length in 3R-MoS₂ has been measured at telecom wavelengths[7]. At L_c (~ 500 nm) the single-pass SHG efficiency is 1.5×10^4 higher than for a monolayer ($I_{2\omega}/I_\omega \approx 10^{-6}$), resulting in the highest conversion efficiency per unit length reported to date for a transparent material[7]. Further increasing this value to achieve macroscopic nonlinear conversion efficiencies, while still preserving the micrometer thickness of TMD crystals, remains an open challenge.

Here we bridge this gap using a non-centrosymmetric van der Waals crystal, 3R-MoS₂, to achieve QPM in periodically-poled transition metal dichalcogenides (PPTMDs). We flip the sign of the optical nonlinearity $\chi^{(2)}$ by stacking consecutive slabs with opposite dipole orientation. The large nonlinearity of TMDs combined with QPM unlocks single-pass conversion efficiencies for SHG higher than 10^{-4} at telecom wavelengths and enables efficient photon-pair generation via SPDC over a microscopic thickness of only $1.2 \mu\text{m}$ – at least two orders of magnitude thinner than BBO and PPLN crystals with similar performances. We observe unique cavity effects prompted by internal reflections of both FW and SH, which increase the conversion efficiency by an additional 50% over standard QPM. Finally, we report the broadband generation of photon pairs at telecom wavelengths via quasi-phase-matched SPDC.

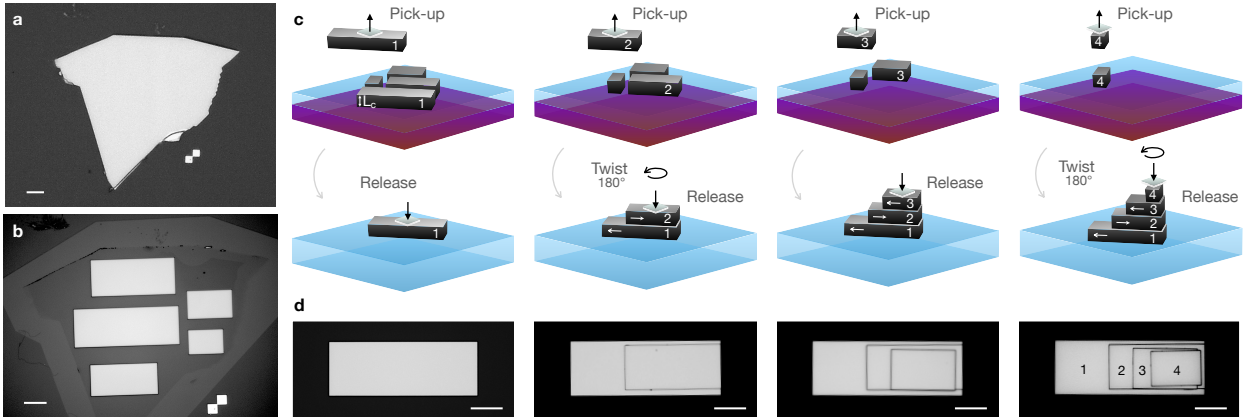


FIG. 1: Periodically poled transition metal dichalcogenides (PPTMDs). (a-b) Micrograph of the 3R-MoS₂ flake (a) before and (b) after patterning (electron beam lithography, etching). (c) Stacking procedure. Slab 1 is first transferred on a $500 \mu\text{m}$ -thick SiO₂ transparent substrate. Slab 2 is twisted by 180° and released on top of slab 1. Slab 3 is transferred on top of slab 2. Finally slab 4 is twisted by 180° and released on top of the 3 stacked portions. (d) Micrographs of each stacking step. Scale bar $10 \mu\text{m}$.

The 3R-MoS₂ crystals are mechanically exfoliated from a commercial bulk 3R-MoS₂ crystal (HQ graphene) grown by chemical vapor transport on a SiO₂/Si substrate. Characterization of the bulk crystal by energy dispersive X-ray analysis and X-Ray diffraction is provided in Ref.[7]. The thickness of the exfoliated flakes

is measured using atomic force microscopy (Supplementary Note 4). To fabricate the PPTMD, we select a large flake with lateral size of $\approx 100 \mu\text{m}$ and thickness $\approx 300 \text{ nm}$, shown in Fig. 1a. We pattern the flake using electron beam lithography and reactive ion etching into smaller portions (Fig. 1b, Supplementary Note 1 for details). By cutting the different slabs out of a single flake, we ensure that all areas have identical thickness and the same macroscopic dipole orientation. Our design and fabrication methodology thus bypasses the need for angle-resolved SHG for crystal orientation characterization.

We choose a flake with thickness of $L_f \approx 300 \text{ nm}$, close to the coherence length L_c measured for a FW at 1450 nm (Supplementary Note 7). The largest portion of the flake (area 1) is transferred onto a $500 \mu\text{m}$ -thick transparent fused silica (SiO_2) substrate, and the other portions (area 2, 3, 4) are individually stacked on top of each other by keeping an interlayer twist angle of 180° [49] (symmetrically equivalent to 60° and 300° twist angles) to flip the sign of $\chi^{(2)}$ at each coherence length (see Fig. 1c), resulting in an overall thickness of $\approx 1.2 \mu\text{m}$ (Supplementary Note 4). The microscope images of the periodically poled crystal at each stacking step are shown in Fig. 1d.

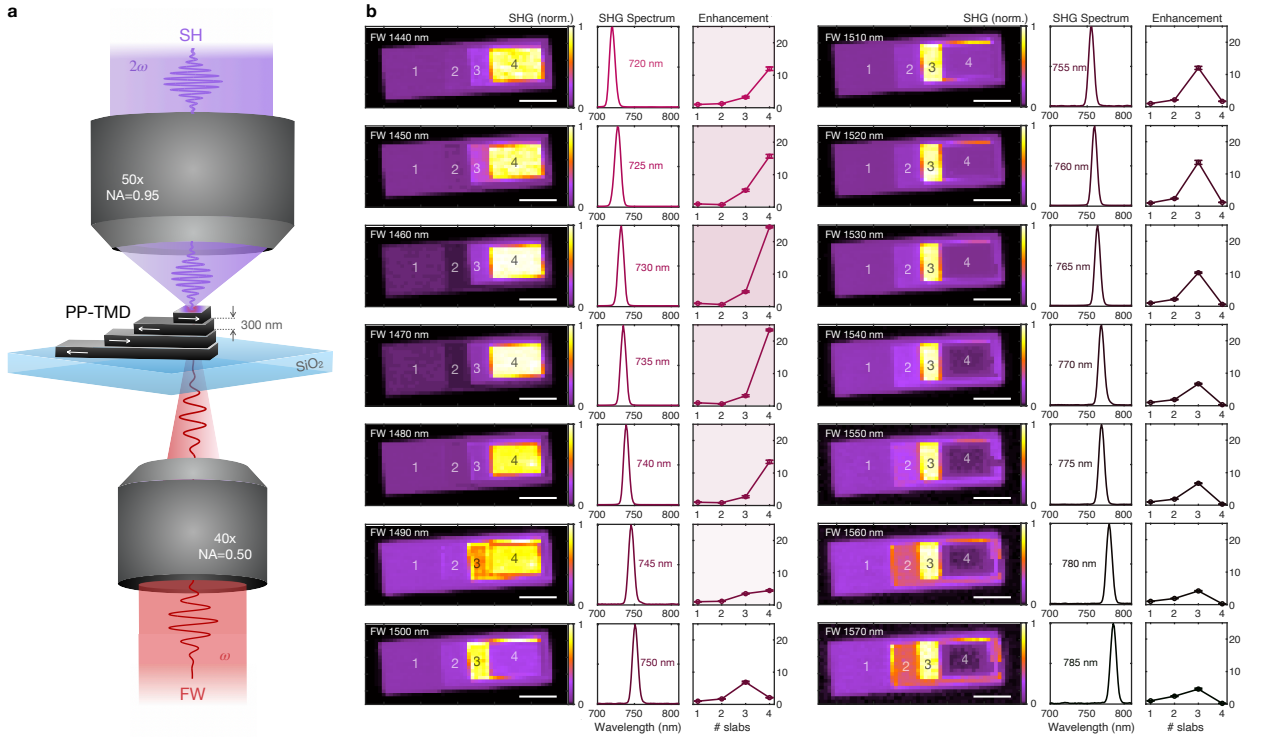


FIG. 2: Pump wavelength-dependent second-harmonic generation from PPTMDs. (a) Transmission microscope. The PPTMD is excited by the FW from the back side of the SiO_2 substrate with a 40x objective. The SH is collected by a 50x objective. (b) Pump wavelength-dependent normalized SH maps of the PPTMD, along with the SH spectra and the SHG enhancement factor with respect to the bare slab. The error bar represents the standard deviation of the SH emission calculated over each corresponding slab area. Scale bar $10 \mu\text{m}$.

To characterize the nonlinear response of the PPTMD, we use a custom-built transmission microscope (Fig. 2a), illuminated by an optical parametric oscillator (OPO, Coherent Chameleon), emitting 150 fs pulses at 80 MHz, tunable in the NIR (1000-1600 nm) wavelength range. We use a long working-distance 40x reflective objective with numerical aperture (NA) 0.5 to focus the FW on the sample from the backside of the substrate. The SH is collected by a 50x objective with a 0.95 NA and directed onto a silicon CCD camera (Supplementary Note 2). The FW is tuned from 1430 nm to 1580 nm, and the power is kept fixed at 0.5 mW (peak power 1.17 GW/cm²). Figure 2b shows the pump wavelength dependent normalized SHG maps, along with the corresponding SHG spectrum. For each pump wavelength, we extract the SH enhancement factor, defined as the SH emission from the regions with 2, 3 and 4 slabs normalized to the SH emission of 1 slab, shown in Fig. 2b. The peak of the SH enhancement is obtained at FW = 1460 nm, at approximately the target operation wavelength for this stack. Compared to a standard first-order QPM ($\chi^{(2)}$ flipped in sign at each coherence length) that predicts a quadratic enhancement of 4, 9 and 16 for 2, 3 and 4 slabs, respectively, the peak enhancement that we obtain is not monotonically increasing with the slab number at each pump wavelength, and it is almost 50% higher in the portion of the stack with 4 slabs. This effect can be explained by considering the modulation of the optical properties caused by interference inside the PPTMD. Multiple reflections of FW and SH radiation at the interfaces between the TMD and the air and glass substrate, acting as optical microcavities, provide nonlinear cavity enhancement effects. To better understand the unconventional QPM regime we observe in PPTMDs, we analytically model our signal by solving the coupled nonlinear equations considering the interference of FW and SH fields in the slabs, and the SH electric field sign inversion for the different poling conditions (Supplementary Note 6). Specifically, we assume that the SH process does not affect the intensity of the FW (undepleted-pump approximation) and we apply the boundary conditions at the entrance and the exit of the TMD slabs to analytically retrieve the interference effects. Calculating the forward and backward propagating FW electric fields and considering the poling, we are able to evaluate the SH in the system. We calculate the second order non linear polarization in the slabs at 2ω induced by FW propagation, and insert this term into Maxwell's equations to extract the SH electric and magnetic fields. Applying again the boundary condition for the SH, we obtain the forward emitted SH intensity. The analytical calculation is performed assuming a normal propagation in the different slabs. A sketch of the modeled structure is shown in Fig. 3a, in which the interference effects of FW and SH are depicted.

Figure 3b and 3c show the measurements and the theoretical simulations of the SH enhancement factor (*i.e.*, SH emission from slab 2, 3 and 4 normalized to the SH from slab 1) as a function of the SH wavelength

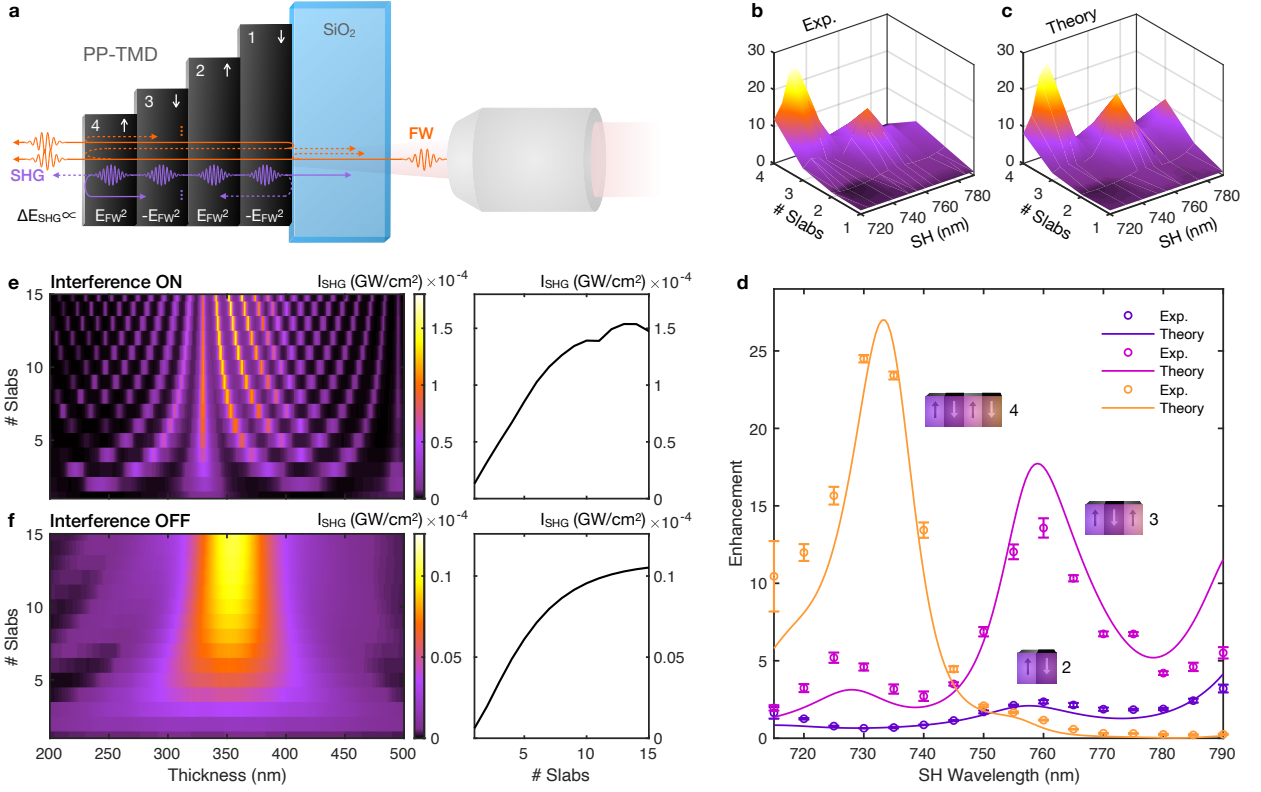


FIG. 3: Theoretical simulations of quasi-phase matching in PPTMDs. (a) Schematic of simulated PPTMD structure. Multiple reflections of FW and SH fields are shown in orange and purple, respectively. The inversion of the electric field at each coherence length is induced by χ^2 flipped in sign via twist-controlled stacking of consecutive slabs. (b) SH enhancement for different wavelengths and number of slabs, as reported in Fig. 2. (c) Corresponding SH enhancement extracted from the model. (d) Quantitative comparison of the wavelength-dependent enhancement between experiment and model for different number of slabs, *i.e.*, cross sections of panel (b) and (c), respectively. (e-f) Calculated SH intensity as a function of slab thickness and number of slabs at FW = 1450 nm and 5 GW/cm² intensity, in two cases: with interference effects of the FW (e), and without interference (f). The maximum intensity achievable as a function of the total number of slabs in the PPTMD is shown on the right, showing that interference boosts SHG, due to intrinsic cavity-induced enhancements.

and the number of slabs, respectively. For the theoretical simulations, we use the refractive index reported in Fig. S2, $|\chi^{(2)}| = 100 \text{ pm/V}$ and a slab thickness equal to 293 nm (Supplementary Note 6). Figure 3d reports the comparison between experiments and theory for poled structures with 2, 3 and 4 slabs, demonstrating a very good agreement with the data. The theoretical model also accurately reproduces the nonlinear response of PPTMDs with different poling periods (Supplementary Note 8). Data and simulations emphasize the importance of an appropriate choice of the number of slabs for each FW wavelength and a given slab thickness, to maximize the enhancement of SH. In particular, for our 300-nm slab thickness, a configuration with 3 slabs provides a higher enhancement compared to the poled structure with 4 slabs for SH wavelengths above 750 nm.

Figure 3e shows the intensity profile of SH for different slab thicknesses and number of slabs, assuming

a FW at 1450 nm, 5 GW/cm^2 peak power and $|\chi^{(2)}| = 100 \text{ pm/V}$. The results show a maximum efficiency for a $L_f \sim 350 \text{ nm}$, with a strong dependence on the interference effects of the FW. The optimum poling period is strongly dependent on the FW. For instance, at 1550 nm the maximum efficiency is achieved for $L_f \sim 550 \text{ nm}$ (see Supplementary Note 6). We also report the same simulation removing the interference of the FW in the slab (Fig. 3f), which we achieve by setting the real part of refractive index of air after the slabs equal to that of the TMD. In this case, the interference pattern is removed, obtaining a more homogeneous profile. However, the maximum efficiency is notably reduced (more than $10\times$ lower). This comparison highlights the key role played by the intrinsic cavity enhancement effects in PPTMDs.

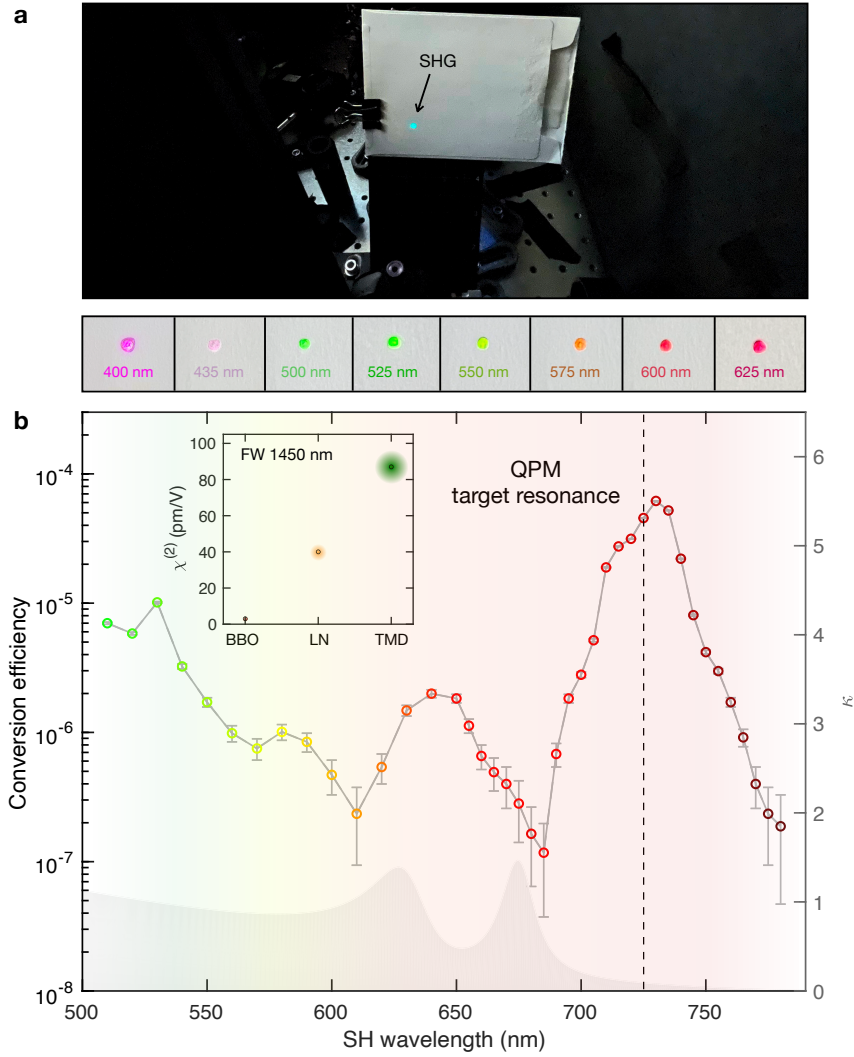


FIG. 4: PPTMD second harmonic conversion efficiency. (a) Picture of the SHG spot at 530 nm, and close-up of the tunable SH from 400 nm to 625 nm. (b) Broadband SH conversion efficiency with tunable pump wavelength (1020 nm - 1580 nm) and fixed power 40 mW (peak power $\approx 90 \text{ GW/cm}^2$). The grey area is the imaginary part of the refractive index κ . In the inset we report the nonlinearity of TMDs ($\chi^{(2)} \approx 100 \text{ pm/V}$), extracted from the conversion efficiency measurements, compared with the one of BBO and LN crystals[1, 50].

We use the frequency tunable OPO to quantitatively measure the wavelength dependent conversion efficiency of the PPTMD. The photographs of the broadly tunable SH spots of our 1.2 μm -thick PPTMD are shown in Fig. 4a. Using a power meter, we measure the SH power emitted by the sample excited with tunable pump and a constant power of 40 mW (peak intensity $\approx 90 \text{ GW}/\text{cm}^2$). The measured conversion efficiency for different excitation wavelengths is shown in Fig. 4b. The peak of the conversion efficiency ($\approx 10^{-4}$) is recorded at $\text{FW} = 1460 \text{ nm}$), *i.e.*, the target phase-matched wavelength with the poling period we use. We stress the fact that this macroscopic conversion efficiency is recorded over a sample thickness of only 1.2 μm . PPTMDs eclipse the previous thickness-conversion efficiency trade-off curves, and now show macroscopic efficiencies over microscopic thicknesses. At the QPM resonance the extracted nonlinearity is $\chi^{(2)} \approx 100 \text{ pm}/\text{V}$ (Supplementary Note 10). With higher $\chi^{(2)}$ compared to BBO/PPLN[1, 50] (see inset of Fig. 4b), PPTMDs achieve the same efficiency, but over approximately 10 – 100 \times shorter propagation lengths.

Finally, we use PPTMDs to demonstrate SPDC. For these measurements, we employ a PPTMD stack with peak enhancement at $\text{FW} = 1420 \text{ nm}$ (Supplementary Note 11). We measure SPDC in this PPTMD using a transmission geometry, as depicted in Fig. 5a. The tunable pump beam is generated by frequency doubling the signal beam of an OPO (Stuttgart Instruments, Alpha). This system provides 170 fs pulses at an 80 MHz repetition rate, with a signal wavelength ranging from 1400 nm to 1600 nm, resulting in doubled wavelengths from 700 to 800 nm. Aspheric lenses before and after the sample (with matched $\text{NA}=0.68$) are used to focus the laser beam onto the sample and collect the resulting SPDC signal. After the PPTMD, the pump beam is filtered out with two hard-coated long-pass filters at a cutoff wavelength of 1150 nm. The SPDC signal can then either be coupled directly into single-mode fiber (SMF28, Corning), or directed towards our setup for spectral characterization. The inset of Fig. 5b shows the expected linear power dependence of the SPDC signal measured with superconducting nanowire single-photon detectors (PhotonSpot). We measure the SPDC spectrum with a birefringent interferometer, the TWINS[51], which is inserted in the optical path of the SPDC signal after which the photons (both the signal and idler) are coupled into multi-mode fiber and detected by an InGaAs single-photon detector (IDQuantique). The setup is described in more detail in Supplementary Note 3.

We collect SPDC spectra for different excitation wavelengths, ranging from 700 nm to 800 nm in steps of 10 nm, from a 4-slabs and from a 1-slab sample. Fig. 5b plots the resulting broadband SPDC spectrum from slab 4 (left) and slab 1 (right). As the signal is significantly stronger from the 4-slabs sample, we use an average pump power of 0.5 mW to acquire the 4-slabs data and 2 mW for the 1-slab data to avoid detector

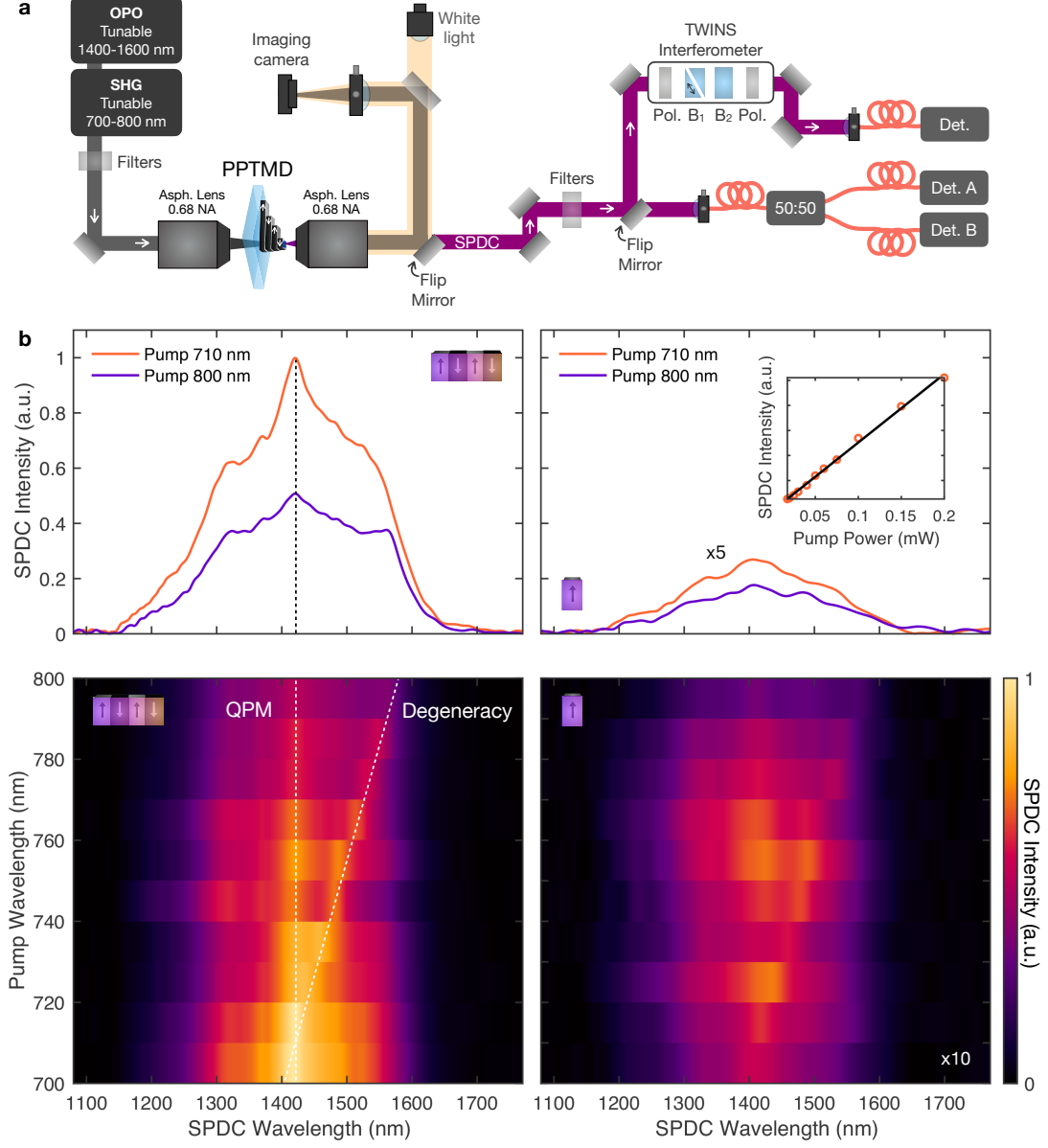


FIG. 5: Pump wavelength-dependent SPDC from PPTMDs. (a) Experimental setup. A frequency-doubled beam from the OPO is used to pump the PPTMD in a transmission geometry. The generated SPDC photons can be directed to a Hanbury Brown-Twiss interferometer in one arm for photon-pair correlation measurements, or to an birefering Fourier transform interferometer (TWINS) for spectral characterization. B1 is a pair of birefringent wedges and B2 is a birefringent plate with optical axis rotated by 90° with respect to the wedges. (b) The upper panels show the SPDC spectra for pump wavelengths of 710nm and 800nm, from the 4-slabs (left) and 1-slab (right, multiplied $\times 5$) samples. The lower panels plot color map illustrating the SPDC spectrum intensity for each pump wavelength from 700 nm to 800 nm, for 4-slabs (left) and 1-slab (right, multiplied $\times 10$) samples. The inset plots the pump power dependence of the SPDC signal (depicted by orange dots), and its corresponding linear fit (black line).

saturation. To account for this, we divide the 4-slabs spectra by four in order to fairly compare the spectra (this is based on the linear power dependence confirmed in the inset). In Fig. 5, we further multiply the

1-slab data by a factor of five and ten in the individual spectra (upper right panel) and in the integrated SPDC map (lower right panel), respectively, to allow for a more direct comparison of the spectral features.

In addition to enhanced efficiency, we note several other features in these spectra. First, we observe a broadband background, which appears to be limited by our detector response. This is to be expected as the SPDC process works around the degeneracy condition, for which the group velocities of the signal and idler waves are matched, resulting in a broad phase-matching bandwidth[52]. The peak corresponding to the degeneracy condition, which shifts with pump wavelength, is shown as a dashed line in the lower panel of the 4-slabs data. Additionally, we plot a vertical dashed line at 1420 nm which corresponds to the QPM peak. Its intensity, relative to the broadband background, grows as the pump is brought into resonance. This is more apparent when comparing the spectra in the upper panel, taken at the resonant wavelength of 710 nm (purple), and the off-resonant spectrum taken at 800 nm (orange). In addition to the QPM peak, we see another peak occurring at the degenerate wavelength (twice the pump wavelength). Because of the less stringent phase-matching conditions, the features are not as visible in the single slab data on the right as they are in the 4-slabs data. We additionally perform correlation measurements on the SPDC signal, measuring a maximum coincidence-to-accidental ratio of 37.3 ± 2.9 when pumping at a non-resonant wavelength (Supplementary Note 11).

In conclusion, we introduce periodically poled van der Waals layered materials as a novel nonlinear platform for classical and quantum light generation. By periodically stacking 3R-MoS₂ slabs with identical thickness and an interlayer twist angle of 180°, we flip the sign of $\chi^{(2)}$ and achieve quasi-phase matching, restoring the proper phase relationship between fundamental and second harmonic, and between fundamental and spontaneously down-converted fields. Due to the large nonlinearity of 3R-TMDs (100-1000 pm/V) we demonstrate a record single-pass second harmonic conversion efficiency of 10^{-4} at telecom wavelengths, over a thickness of only 1.2 μm (two poling periods). Moreover, in the phase-matched interaction, we observe nonlinear enhancement which surpasses by more than 50% the usual quadratic enhancement typically observed in standard quasi-phase-matched crystals. This is attributed to cavity effects, which enhance the field overlap inside the periodically poled structure. Theoretical simulations accurately reproduce the conditions for such an unconventional quasi-phase matching, and predict the optimal slab thickness as a function of the FW/SH wavelength (Supplementary Note 6). Although the sample has been prepared by manual exfoliation and stacking, the periodic poling process is potentially scalable, as it can be automatized using a robotic stacking machine[53] (Supplementary Note 5). PPTMDs now provide macroscopic nonlinear

conversion efficiencies over microscopic thicknesses, establishing new routes for designing novel nonlinear optical devices and quantum nanophotonic circuit elements[54], such as entangled-photon generators directly embedded on chip.

DATA AVAILABILITY

All data generated or analysed during this study, which support the plots within this paper and other findings of this study, are included in this published article and its Supplementary Information. Source data are provided with this paper.

ACKNOWLEDGEMENTS

We thank Benedikt Ursprung for useful discussions.

This work was supported by Programmable Quantum Materials, an Energy Frontier Research Center funded by the US Department of Energy, Office of Science, Basic Energy Sciences, under Award DE-SC0019443. C.T. acknowledges the European Union’s Horizon Europe research and innovation programme under the Marie Skłodowska-Curie PIONEER HORIZON-MSCA-2021-PF-GF grant agreement No 101066108. C.T. also acknowledges the Optica Foundation and Coherent Inc. for supporting this research through the Bernard J. Couillaud prize 2022. G.C acknowledges support by the Progetti di ricerca di Rilevante Interesse Nazionale (PRIN) of the Italian Ministry of Research 2022HL9PRP Overcoming the Classical limits of ultrafast spectroscopy with entangled photons (CRESCENDO). A.M. acknowledges funding from the European Union—NextGenerationEU under the Italian Ministry of University and Research (MUR) National Innovation Ecosystem Grant No. ECS00000041-VITALITY-CUP E13C22001060006, and Progetti di ricerca di Rilevante Interesse Nazionale (PRIN) of the Italian Ministry of Research PHOTO (Photonic Terahertz devices based on topological materials) No. 316 2020RPEPNH. A.Y. acknowledges support from the Department of Defense (DoD) through the National Defense Science and Engineering Graduate (NDSEG) Fellowship Program. J.P. acknowledges funding from the Air Force Office of Scientific Research (FA9550-21-1-0323) and the Office of Naval Research (N000142212841). P.W. acknowledges support from the Austrian Science Fund (FWF) through BeyondC (F7113) and from AFOSR via FA8655-20-1-7030 (PhoQuGraph) and FA8655-23-1-7063 (TIQI); and from the Austrian Federal Ministry for Digital and Economic Affairs,

the National Foundation for Research, Technology and Development and the Christian Doppler Research Association.

Author contributions

C.T. conceived the experiment and performed the measurements. C.F. and A.M. developed the theory model. J.B., B.B., C.T. and P.K.J. performed the spontaneous parametric down-conversion measurements. B.Y., C.T., Z.P., X.X. and A.Y. prepared the samples. X.X., C.T. and Z.P. built the experimental setup and performed the morphological characterization of the samples. M.D., D.N.B, J.P., L.A.R., P.W., C.D., G.C. and P.J.S. supervised the study. C.T. wrote the manuscript with input from all authors.

Competing interests

The authors declare no competing interests.

Additional information

REFERENCES

- [1] Boyd, R. W. *Nonlinear Optics. Academic Press.* (2020).
- [2] Elshaari, A.W., et al. Hybrid integrated quantum photonic circuits. *Nat. Photonics* **14**, 285–298 (2020).
- [3] Boes, A. et al. Lithium niobate photonics: Unlocking the electromagnetic spectrum. *Science*. **379**, eabj4396 (2023).
- [4] Fejer, M. M., Jundt, D. H., Byer, R. L. & Magel, G. A. Quasi-phase-matched second harmonic generation: tuning and tolerances. *IEEE Journal of Quantum Electronics*. **28**, 2631 – 2654 (1992).
- [5] Zhao, M. et al. Atomically phase-matched second-harmonic generation in a 2D crystal. *Light: Science & Applications*. **5**, e16131–e16131 (2016).

- [6] Shi, J. et al. 3R MoS₂ with Broken Inversion Symmetry: A Promising Ultrathin Nonlinear Optical Device. *Adv. Mater.* **29**, 1701486 (2017).
- [7] Xu, X. et al. Towards compact phase-matched and waveguided nonlinear optics in atomically layered semiconductors. *Nat. Photon.* **16** 698–706 (2022).
- [8] Wang, C. et al. Ultrahigh-efficiency wavelength conversion in nanophotonic periodically poled lithium niobate waveguides. *Optica.* **5**, 1438–1441 (2018).
- [9] Suntsov, S., Rüter, C. E., Brüske, D. & Kip, D. Watt-level 775 nm SHG with 70% conversion efficiency and 97% pump depletion in annealed/reverse proton exchanged diced PPLN ridge waveguides. *Opt. Express.* **29**, 11386–11393 (2021).
- [10] Santiago-Cruz, T. et al. Resonant metasurfaces for generating complex quantum states. *Science.* **377**, 991–995 (2022).
- [11] Shih, Y. An Introduction to Quantum Optics Photon and Biphoton Physics. *Taylor & Francis.* (2016).
- [12] Myers, L. E. et al. Quasi-phase-matched optical parametric oscillators in bulk periodically poled LiNbO₃. *Journal of the Optical Society of America B.* **12**, 2102–2116 (1995).
- [13] Koh, S. et al. Sublattice Reversal in GaAs/Si/GaAs (100) Heterostructures by Molecular Beam Epitaxy. *Jpn. J. Appl. Phys.* **37**, L1493 (1998).
- [14] Eyres, L. A. et al. All-epitaxial fabrication of thick, orientation-patterned GaAs films for nonlinear optical frequency conversion. *Appl. Phys. Lett.* **79**, 904–906 (2001).
- [15] Grisard, A. et al. Fabrication and applications of orientation-patterned gallium arsenide for mid-infrared generation. *Physica Status Solidi (C).* **9**, 1651–1654 (2012).
- [16] Gordon, L. et al. Diffusion-bonded stacked GaAs for quasiphasematched second-harmonic generation of a carbon dioxide laser. *Electronics Letters.* **29**, (1993).
- [17] Tanimoto, R., Takahashi, Y. & Shoji, I. Quasi-phase-matching stack of 25 GaAs plates with high transmittance for high-power mid-infrared wavelength conversion fabricated by use of room-temperature bonding. *Physica Status Solidi (C).* **38**, (2021).
- [18] Feng, D. et al. Enhancement of second-harmonic generation in LiNbO₃ crystals with periodic laminar ferroelectric domains. *Appl. Phys. Lett.* **37**, (1980).
- [19] Feisst, A. & Koidl, P. Current induced periodic ferroelectric domain structures in LiNbO₃ applied for efficient nonlinear optical frequency mixing. *Appl. Phys. Lett.* **47**, (1985).
- [20] Matsumoto, S., Lim, E. J., Hertz, H. M. & Fejer, M. M. Quasiphasematched second har-

- monic generation of blue light in electrically periodically-poled lithium tantalate waveguides. *Electronics Letters*. **27**, (1991).
- [21] Van Der Poel, C. J., Bierlein, J. D., Brown, J. B. & Colak, S. Efficient type I blue second-harmonic generation in periodically segmented KTiOPO₄ waveguides. *Appl. Phys. Lett.* **57**, 20 (1990).
- [22] Hum, D. S. & Fejer, M. M. Quasi-phasematching. *Comptes Rendus Physique*. **8**, (2007).
- [23] Myers, L. E. & Bosenberg, W. R. Periodically poled lithium niobate and quasi-phase-matched optical parametric oscillators. *IEEE Journal of Quantum Electronics*. **33**, 10 (1997).
- [24] Yang, S. T. & Velsko, S. P. Frequency-agile kilohertz repetition-rate optical parametric oscillator based on periodically poled lithium niobate. *Opt. Lett.* **24**, 133–135 (1999).
- [25] Lu, J. et al. Ultralow-threshold thin-film lithium niobate optical parametric oscillator. *Optica*. **8**, 539–544 (2021).
- [26] Ledezma, L. et al. Octave-spanning tunable infrared parametric oscillators in nanophotonics. *Sci. Adv.* **9**, eadf9711 (2023).
- [27] Solntsev, A. S. et al. LiNbO₃ waveguides for integrated SPDC spectroscopy. *APL Photonics*. **3**, 10 (2018).
- [28] Zhang, C. et al. Spontaneous Parametric Down-Conversion Sources for Multiphoton Experiments. *Adv. Quantum Technol.* **4**, 2000132 (2021).
- [29] Krasnok, A., Tymchenko, M. & Alù, A. Nonlinear metasurfaces: a paradigm shift in nonlinear optics. *Materials Today*. **21**, 8–21 (2018).
- [30] Wang, K., Chekhova, M., & Kivshar, Y. Metasurfaces for quantum technologies. *Physics Today*. **75**, 3745–3763 (2022).
- [31] Fedotova, A. et al. Lithium Niobate Meta-Optics. *ACS Photon.* **9**, 3745–3763 (2022).
- [32] Neshev, D. N. & Miroshnichenko, A. E. Enabling smart vision with metasurfaces. *Nat. Photon.* **17**, 26–35 (2023).
- [33] Zhu, S. et al. Integrated photonics on thin-film lithium niobate. *Adv. Opt. Photon.* **13**, 242–352 (2021).
- [34] Jankowski, M. et al. Supercontinuum generation by saturated second-order nonlinear interactions. *APL Photonics*. **8** 116104 (2023).
- [35] Guo, Q., et al. Ultrathin quantum light source with van der Waals NbOCl₂ crystal. *Nature* **613** 53–59 (2023).

- [36] Wu, L., et al. Giant anisotropic nonlinear optical response in transition metal monpnictide Weyl semimetals. *Nat. Physics* **13** 350–355 (2017).
- [37] Mueller, T. & Malic, E. Exciton physics and device application of two-dimensional transition metal dichalcogenide semiconductors. *npj 2D Mater. Appl.* **2** 29 (2018).
- [38] Du, L. et al. Moiré photonics and optoelectronics. *Science* **379** eadg0014 (2023).
- [39] Ma, Q. et al. Photocurrent as a multiphysics diagnostic of quantum materials. *Nat. Rev. Phys.* **5** 170–184 (2023).
- [40] Sheffer, Y., Queiroz, R. & Stern, A. Symmetries as the Guiding Principle for Flattening Bands of Dirac Fermions *Phys. Rev. X* **13** 021012 (2023).
- [41] Malard, L. M. et al. Observation of intense second harmonic generation from MoS2 atomic crystals. *Phys. Rev. B.* **87** 201401 (2013).
- [42] Li, Y. et al. Probing Symmetry Properties of Few-Layer MoS2 and h-BN by Optical Second-Harmonic Generation. *Nano Lett.* **13**, 3329–3333 (2013).
- [43] Wang, G. et al. Giant enhancement of the optical second-harmonic emission of WSe2 monolayers by laser excitation at exciton resonances. *Phys. Rev. Lett.* **114** 097403 (2015).
- [44] Autere, A. et al. Nonlinear Optics with 2D Layered Materials. *Adv. Mater.* **30**, 1705963 (2018).
- [45] Wen, X., Gong, Z. & Li, D. et al. Nonlinear optics of two-dimensional transition metal dichalcogenides. *Wiley Online Library.* **1**, 317–337 (2019).
- [46] Liu, W. et al. Recent Advances of 2D Materials in Nonlinear Photonics and Fiber Lasers. *Adv. Optical Mater.* **8**, 1901631 (2020).
- [47] Dogadov, O. et al. Parametric Nonlinear Optics with Layered Materials and Related Heterostructures. *Laser & Photonics Reviews.* **16**, 2100726 (2022).
- [48] Trovatiello, C. et al. Optical parametric amplification by monolayer transition metal dichalcogenides. *Nat. Photonics.* **15**, 6–10 (2021).
- [49] Hong, H. et al. Twist-phase-matching in two-dimensional materials. *arXiv*, 2305.11511 (2023).
- [50] Schiek, R. & Pertsch, T. Absolute measurement of the quadratic nonlinear susceptibility of lithium niobate in waveguides. *Opt. Mater. Express* **2**, 126–139 (2012).
- [51] Brida, D. et al. Phase-locked pulses for two-dimensional spectroscopy by a birefringent delay line. *Opt. Lett.* **37**, 3027–3029 (2012).
- [52] Manzoni, C. & Cerullo, G. Design criteria for ultrafast optical parametric amplifiers. *J. Opt.* **18**, 103501 (2016).

- [53] Mannix, A. J., Ye, A. et al. Robotic four-dimensional pixel assembly of van der Waals solids. *Nat. Nanotechnol.* **17**, 361–366 (2022).
- [54] Li, H. et al. Probing dynamical symmetry breaking using quantum-entangled photons. *Quantum Science and Technology.* **3**, 015003 (2017).